PCCP

PAPER

View Article Online
View Journal | View Issue

Cite this: *Phys. Chem. Chem. Phys.*, 2023, **25**, 26065

Growth of a quasicrystal-related structure and superstructure for ultrathin Ce–Ti–O films on Pt(111)

Xu Li, *[a] Lap Hong Chan,[a] Sho-ichi Takakura,[b] Masashi Nakatake,[b] Tsunetomo Yamada,[c] Ryuji Tamura[d] and Junji Yuhara[a]

Received 27th June 2023,
Accepted 1st September 2023

DOI: 10.1039/d3cp03013j

rsc.li/pccp

Herein, oxide quasicrystal-related (OQC-R) structure and Ce–Ti–O-(3 × 3) superstructure ultrathin films were prepared on Pt(111) and characterized using scanning tunneling microscopy (STM) and low-energy electron diffraction. The OQC-R structure with dodecagonal clusters consisting of triangles, squares, and rhombuses was observed in STM images. The first discovery of the OQC-R structure with a magnetic rare earth metal expands the possibility of discovering new oxide quasicrystals with novel magnetism or superconductivity. By depositing Ti on an OQC-R ultrathin film and post-annealing, a honeycomb lattice of the Ce–Ti–O-(3 × 3) superstructure was prepared. From X-ray photoelectron spectroscopy (XPS) and resonant-photoelectron spectroscopy, the chemical states of the Ce and Ti atoms in the OQC-R structure corresponded to the Ce^{3+} and Ti^{2+} states, while those for the Ce–Ti–O-(3 × 3) superstructure corresponded to the Ce^{3+}, Ti^{3+}, and Ti^{2+} states. The phase transformation from the OQC-R structure to the Ce–Ti–O-(3 × 3) honeycomb superstructure likely occurred when the amount of Ti increased and was more oxidized. The elemental atomic density was also calibrated using XPS and Rutherford backscattering spectroscopy. These results propose tentative structural models of the OQC-R structure as $Ce_{18}Ti_{14}O_{41}$ and the Ce–Ti–O-(3 × 3) superstructure as $CeTi_6O_9$.

I Introduction

Quasicrystals were first discovered in 1984 by D. Shechtman.[1] Then, in 2013, Förster *et al.* reported oxide quasicrystals (OQCs) prepared from an ultrathin Ba–Ti–O film on Pt(111).[2] The 12-fold quasi-periodicity was confirmed using scanning tunneling microscopy (STM) and low-energy electron diffraction (LEED). The dodecagonal cluster of the OQC structure has 12 triangles, 5 squares, and 2 rhombuses. Later, in 2017, Schenk *et al.* reported the OQC structure of the same dodecagonal cluster for an ultrathin Sr–Ti–O film on Pt(111).[3]

Along with the OQC structure, the oxide crystalline approximant (OCA) structure has also been reported. The OCA structure has a periodic arrangement of characteristic building blocks inherent in the OQC structure. For example, an 8°-rotated Sigma phase OCA of Ba–Ti–O has been prepared on Pt(111), Ru(0001), or Pd(111) surfaces.[4–6] Our group also prepared 8°-rotated Sigma phase OCA and OQC structures of Ba–Ti–O on Pt(111).[7,8] In addition, structural models, in which Ba atoms were located at the corners of the tiling, were proposed based on the atomic density, the chemical bonding state of each element, and the symmetry and protrusions of the STM images.

For a given OQC structure, there are usually various OCA structures with different structural complexity. Recently, two new complex phases, rectangular and hexagonal approximants, were reported by C. R. Merchan *et al.*[9] These two approximants were obtained by reducing $SrTiO_3$ on a Pt(111) buffer layer, which was grown on a sapphire(0001) substrate. In addition to the OCA structure, another structure related to the OQC structure exists, called an oxide quasicrystal-related (OQC-R) structure herein. This structure has a crystal periodicity-like OCA, and part of it contains the same tiles, such as triangles, squares, and rhombuses, as quasicrystals. However, the tiles are not included in the quasicrystals but appear in the unit cell. Like the Ba–Ti–O ultrathin film prepared on the Pt(111) substrate,[10] in the unit cell, a trapezoid that did not exist in the OQC tiling was observed in the STM image of the OQC-R structure.

However, OQC structures based on ultrathin $BaTiO_3$ and $SrTiO_3$ films on Pt(111) have already been fabricated; hence, we changed Ba/Sr to other metal elements. We aimed to prepare an OQC structure with new clusters or related structures, such as

[a] *Department of Energy Engineering, Nagoya University, Nagoya 464-8603, Japan. E-mail: li.xu.w8@s.mail.nagoya-u.ac.jp*
[b] *Aichi Synchrotron Radiation Center, Seto, Aichi 489-0965, Japan*
[c] *Department of Applied Physics, Tokyo University of Science, Tokyo 125-8585, Japan*
[d] *Department of Materials Science and Technology, Tokyo University of Science, Tokyo 125-8585, Japan*

the OCA structure, using rare-earth metals next to Ba on the periodic table. Herein, Ba was replaced with Ce owing to the similar lattice constant of $CeTiO_3$ (0.3939 nm) to $BaTiO_3$ (0.4088 nm) and $SrTiO_3$ (0.3905 nm).[3,11] In compounds, Ce tends to form Ce^{3+} with one 4f electron. As a result, Ce compounds have a magnetic order, superconducting state, and heavy electronic state in proximity owing to the relationship between the conduction electrons with the $4f^1$ state. Furthermore, the magnetic order to the superconducting state can be controlled by applying pressure.[12,13] In addition, the OQC and OCA structures of Ba–Ti–O are reduced oxides, and Ti always corresponds to Ti^{3+} and Ti^{2+}. Theoretically, the OQC and OCA structures of rare-earth metals may have magnetism and are expected to be ferromagnetic, antiferromagnetic, or superconducting materials.

Therefore, the growth and structures of ultrathin Ce–Ti–O films on Pt(111) will be reported herein. The OQC-R structure and Ce–Ti–O-(3 × 3) superstructure of ultrathin Ce–Ti–O films were prepared, as confirmed using STM and LEED. The atomic composition ratios, chemical bonding state, and atomic density of Ce, Ti, and O in both structures were determined. According to these experimental results, the structural models are proposed.

II Experiment

A clean Pt(111) crystal was prepared using 2 keV Ar^+-ion sputtering at room temperature, followed by annealing at 1000 °C in an ultrahigh vacuum (UHV) chamber. To remove carbon from Pt(111), the sample was also annealed at 900 °C and cooled down to 400 °C in the O_2 atmosphere repeatedly, until the absence of carbon was confirmed using X-ray photoelectron spectroscopy (XPS), Auger electron spectroscopy (AES), and LEED.

The ultrathin Ce–Ti–O film was prepared after Ce and Ti deposition on a cleaned Pt(111) surface, following by annealing at 900 °C for 5 min in an O_2 atmosphere under 3×10^{-6} mbar, and post-annealed under UHV at 900 °C to 1000 °C for 5 min. Ce was deposited using a handmade evaporator, setting a Ce block wrapped in a W filament, and Ti was deposited using an electron bombardment evaporator (EFM3, Omicron). The details of the evaporator setup for Ce and Ti can be found elsewhere.[7,8,14] The periodicity and morphology of the ultrathin films were determined using LEED (LaB_6 filament, 4-grid, Omicron) and STM (STM-1, Omicron). The compositional ratio was calculated from the peaks of each element in the AES spectra. The sensitivity factors were abstracted from the AES handbook,[18] and are 0.3 for Ce-NON (82 eV), 0.44 for Ti-LMM (418 eV), and 0.5 for O-KLL (503 eV). XPS (Mg Kα X-ray) and Rutherford backscattering spectroscopy (RBS) calibrated the elemental atomic density. For the RBS measurement, we prepared the Ce–O or Ba–Ti–O ultrathin films on the polycrystalline graphite substrate to obtain the relationship between XPS intensity and elemental atomic density. The details of RBS have been published elsewhere.[7,14] The resonant-photoelectron spectroscopy (resonant-PES) and soft X-ray absorption spectroscopy (XAS) analyses were conducted in the Beamline 7U at the Aichi Synchrotron Radiation Center. The spectra were recorded using an MBS A1 electronic energy analyzer in a UHV chamber under 2×10^{-10} mbar, with the energy resolution (E/△E) of 7×10^3. Resonant-PES measurements were carried out with 121 eV, 114 eV, and 113.5 eV photons. The pass energy is set to 50 eV, with an angle of 90° between the incident X-ray and the sample. For the XAS analyses, the total electron yield was measured using an energy resolution of 0.2 eV at the M4,5 edges ($h\nu \approx$ 878–915 eV). The angles between the incident X-ray and the sample were 15° and 90°.

III Experimental results

Fig. 1 shows the OQC-R ultrathin Ce–Ti–O film on Pt(111), which is prepared by depositing 0.5 ML Ce and 0.8 ML Ti, followed by annealing at 900 °C for 5 min in an O_2 atmosphere under 3×10^{-6} mbar, and post-annealed under UHV at 900 °C for 5 min. Here, 1 ML is defined as the topmost layer with an atomic density of the Pt(111) layer of 1.5×10^{15} atoms per cm^2. Fig. 1(a) shows the wide-scale STM image of the OQC-R structure. A wide terrace and Pt(111) atomic layer step can be observed in the STM image. Small bright spots are observed on the terrace, ranging from 0.58 to 1.36 nm in height, and are considered to be formed by Ce–Ti–O.[15] Fig. 1(b) shows the STM image at 35 × 35 nm^2 comprising irregular protrusions in a large area. Fig. 1(c) displays the atomically resolved STM image of the OQC-R structure from the region marked by a black square shown in Fig. 1(b). An arrangement of the dodecagons is observed, which consists of triangles and squares marked in white. The average distance between the protrusions is 0.64 nm, and the average height of the protrusions is 0.09 nm. These dodecagons form a large unit cell with a side length of 3.8 nm marked as a red rhombus. In addition, there are triangles with two orientations in the center of the dodecagons, which are marked in purple. These purple triangles have an unequal distance to the clusters, which are marked in white, leading to the appearance of a trapezoid. Thus, we cannot strictly call the resultant structure an OCA structure, but an OQC-R structure. At the dodecagon junctions, there are also triangles, quadrilaterals and rhombuses. Based on the cluster marked in white, the arrangement of some protrusions in the clusters seems to form a distorted sigma phase locally, marked in blue. We can also find the arrangement of triangles from another view angle, as displayed in Fig. 1(d). The STM images have three types of triangles, marked in red, purple, and green. The arrangement of these triangles presents a periodic distribution. These triangles are arranged along the yellow lines marked as L_1, L_2, and L_3. The fast Fourier transform (FFT) of the STM image is inset in the upper right corner of Fig. 1(c). Six equivalent spots are observed in the center, indicating a single domain of the OQC-R structure. Fig. 1(e) shows the lines profile along the L_1 yellow line in Fig. 1(d). The average height of the protrusions is calculated to be 0.09 nm. The calculated distance of yellow lines is 1.15 nm, corresponding to the yellow spots in the LEED pattern shown in Fig. 1(f). The LEED pattern shows

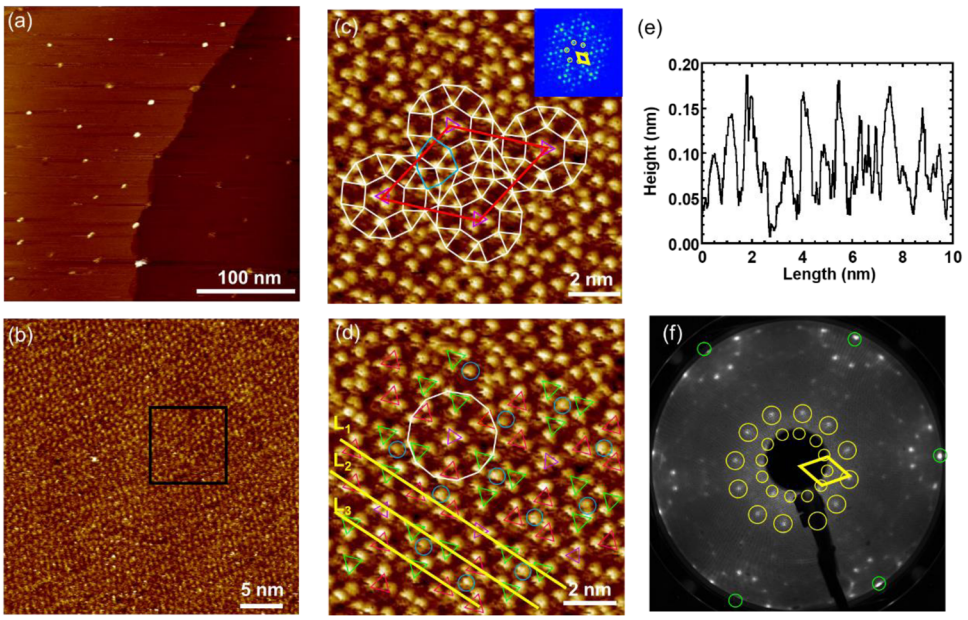

Fig. 1 The OQC-R structure of the ultrathin Ce–Ti–O film prepared using 0.5 ML Ce and 0.8 ML Ti depositions on Pt(111), followed by annealing at 900 °C for 5 min in an O_2 atmosphere at 3×10^{-6} mbar, and post-annealing under UHV at 900 °C for 5 min. (a) The STM image at 300 × 300 nm^2, in a constant current mode with a tunneling current of 300 pA and a sample bias voltage of +1.5 V. (b) The STM image at 35 × 35 nm^2, 300 pA, 0.5 V. (c) and (d) Atomically resolved STM image from the black square in (b), at 9 × 9 nm^2, 300 pA, −0.4 V. The unit cell (red), cluster (white), distorted sigma phase (blue), and yellow lines are marked. The inset in the upper right corner is the FFT of (c). (e) Line profile along the L_1 yellow line in (d). (f) LEED pattern at an incident energy of 45 eV. The Pt(111) primitive (1 × 1) spots are marked with green circles, and the spots corresponding to the OQC-R structure are marked with yellow circles.

that the yellow lines form a rotation of 15° to the Pt(111) substrate. Compared with the yellow lines, the red unit cell formed a rotation of 2° to the Pt(111) substrate. These spots in FFT also agree with the yellow spots in the LEED pattern. Notably, the arrangement of the dodecagons is local. However, the triangles with different directions are well-ordered in a large area as shown in Fig. 1(b), so only the corresponding spots of the triangular arrangement can be observed clearly in the FFT and LEED pattern.

Fig. 2 shows the ultrathin Ce–Ti–O film of the (3 × 3) superstructure on Pt(111), which was prepared by depositing 1 ML Ti on the OQC-R ultrathin Ce–Ti–O film, followed by annealing at 900 °C for 5 min in an O_2 atmosphere, and post-annealed under UHV at 1000 °C for 5 min. In the wide-scale STM image shown in Fig. 2(a), there are many three-dimensional islands (3D) with a height of 0.32–1.92 nm. Compared with the OQC-R structure of the wide-scale STM image shown in Fig. 1(a), Ce–Ti–O likely coagulate, easily forming a 3D island. As shown in Fig. 2(b), the protrusions on the surface have an orderly periodic arrangement. Fig. 2(c) shows the line profile along the white line in Fig. 2(b). The calculated length of the unit cell marked in blue is 1.04 nm, indicating a Pt(111)–Ce–Ti–O-(3 × 3) superstructure. The STM image indicated that the Ce–Ti–O-(3 × 3) superstructure forms a honeycomb lattice, corresponding to the blue spots in the LEED pattern and FFT, as shown in Fig. 2(d) and in the upper right corner of Fig. 2(b). In the LEED pattern, additional spots marked in red are observed. These spots are Ce–Ti–O-(3 × 3) spots that backfolded the Pt(111) hexagonal substrate, which also confirmed that the

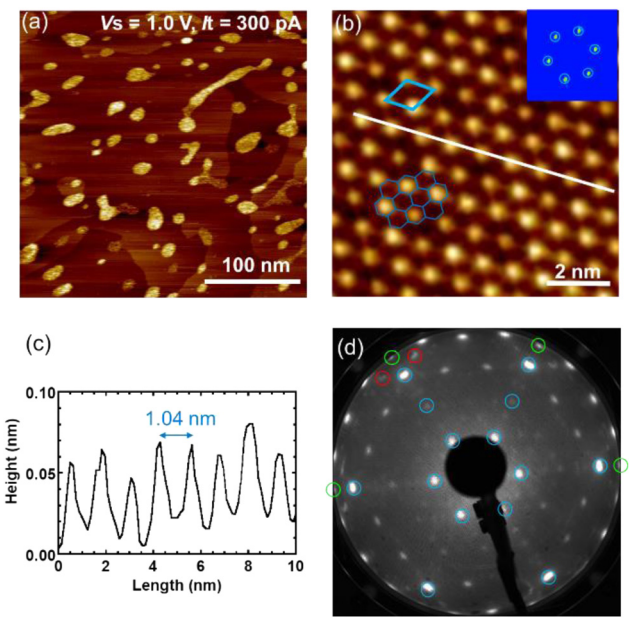

Fig. 2 The Ce–Ti–O-(3 × 3) superstructure of the ultrathin Ce–Ti–O film prepared *via* depositing 1 ML Ti on the OQC-R ultrathin Ce–Ti–O film, followed by annealing at 900 °C for 5 min in an O_2 atmosphere, and post-annealed under UHV at 1000 °C for 5 min. (a) The STM image at 300 × 300 nm^2, 300 pA, +1.0 V. (b) The STM image at 9 × 9 nm^2, 300 pA, +1.5 V. The inset in the upper right corner is the FFT of (b). (c) Line profile along the white line in (b). (d) LEED pattern, 45 eV. The spots corresponding to the Ce–Ti–O-(3 × 3) superstructure are marked with blue circles, and the backfolded Ce–Ti–O-(3 × 3) spots are marked with red circles.

Ce–Ti–O-(3 × 3) superstructure is parallel to the Pt(111) substrate but not commensurate with the Pt(111) substrate.

Fig. 3 shows the AES and XPS spectra of the OQC-R structure and Ce–Ti–O-(3 × 3) superstructure. From the AES spectra shown in Fig. 3(a), the calculated compositional ratio (Ce : Ti : O) of the OQC-R structure and Ce–Ti–O-(3 × 3) superstructure is 1.0 : 0.3 : 0.8, and 1.0 : 0.8 : 1.6, respectively. Fig. 3(b) shows the XPS spectra of Ce 3d core levels. The Ce 3d XPS region generally contains twelve peaks originating from different cerium oxidation states (Ce^{3+} and Ce^{4+}) and the coexistence of different final states. The corresponding photoemission peaks for Ce 3d are summarized in Table 1.[14,16,17] In Table 1, there are also two small peaks that are difficult to observe, marked as S at 895.7 eV and S′ at 914.0 eV, which indicate Ce^{3+} shake-up satellites.[14,16,18] The Ce $3d_{5/2}$ binding energy of the OQC-R structure and Ce–Ti–O-(3 × 3) superstructure is 885.8 eV and 881.5 eV, respectively. Compared with Table 1, Fig. 3(b) demonstrates that both structures exhibit a Ce^{3+} state. From the XPS spectra of the Ti 2p core levels shown in Fig. 3(c), the amount of Ti in the Ce–Ti–O-(3 × 3) superstructure is larger than that in the OQC-R structure. From the report by V. V. Atuchin *et al.*, the binding energies of metallic Ti, Ti^{2+}, Ti^{3+}, and Ti^{4+} are 454, 455.1, 457.8, and 458.9 eV, respectively.[18] Therefore, the observed binding energy of 455.5 eV for the OQC-R structure indicates the main state of Ti^{2+}. In addition, the main peaks observed for the Ce–Ti–O-(3 × 3) superstructure are located at 457.9 and 455.5 eV, indicating the main state of Ti^{3+} and Ti^{2+}. By comparing the peak areal intensity ratio of O/Pt in Fig. 3(c), the OQC-R structure was found to contain less oxygen and was in a further reduced state. The relationship between the XPS intensity and the elemental atomic density obtained from RBS and XPS[7,14] determines the atomic density of Ce, Ti and O atoms in both structures. The elemental atomic density of Ce, Ti, and O atoms is determined to be $(7 \pm 3) \times 10^{14}$, $(4 \pm 2) \times 10^{14}$, and $(5 \pm 1) \times 10^{14}$ atoms per cm^2 for the OQC-R structure ultrathin film and $(5 \pm 3) \times 10^{14}$, $(7 \pm 2) \times 10^{14}$, and $(8 \pm 1) \times 10^{14}$ atoms per cm^2 for the Ce–Ti–O-(3 × 3) superstructure ultrathin film, respectively. Notably, as mentioned in Fig. 2(a), since there are 3D islands on the Ce–Ti–O-(3 × 3) superstructure ultrathin film, the atomic density calculated here also includes these 3D islands.

Fig. 4(a) and (b) shows the valence-band Ce 4d–4f resonant-PES spectra of the OQC-R structure and Ce–Ti–O-(3 × 3) superstructure. For Ce 4f electrons, the Ce 3d–4f resonance is generally sensitive in bulk, whereas 4d–4f is sensitive in thin films.[19] For both structures, the Ce^{3+} peaks are observed at 2.2 eV, but the Ce^{4+} peak is not observed at 4.6 eV. In addition, the areal intensity of the Ce^{3+} peaks indicates that the Ce amount in the OQC-R structure is more than that in the Ce–Ti–O-(3 × 3) superstructure. These results agree with the results obtained using XPS spectra. The areal intensity of the O 2p peak differs from the incident energies because of the cross section of O 2p. For bulk materials, the M4 ($h\nu$ = 877–887 eV) and M5 ($h\nu$ = 895–905 eV) spectra for the pure $|J_z| >$ states of the Ce^{3+} with $4f^1$ are considered with two polarizations of the electric field vector, in parallel or vertical to the *c* axis, based on ionic calculations, which include the full multiplet theory.[20] Each state has a characteristic strong polarization dependence. Such a polarization dependence is related to the spatial distribution of 4f

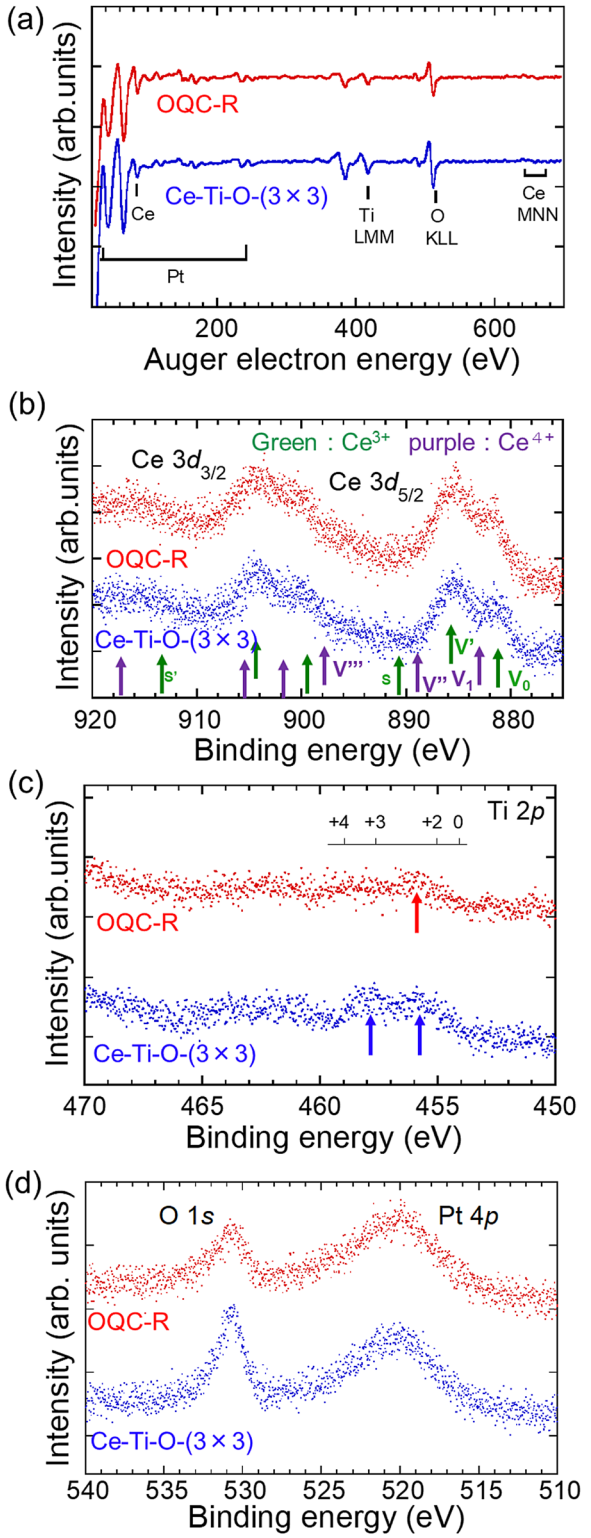

Fig. 3 The AES spectra and XPS spectra of OQC-R structure (red) and Ce–Ti–O-(3 × 3) superstructure (blue) ultrathin films. (a) AES spectra. (b) The XPS spectra of Ce 3d. (c) The XPS spectra of Ti 2p. (d) The XPS spectra of O 1s.

Table 1 The corresponding photoemission peaks for Ce 3d[14,15,17]

		Final state	$3d_{5/2}$ (eV)	$3d_{3/2}$ (eV)
Ce^{3+}	V_0	$3d^9\ 4f^2\ 5d^0\ 6s^0$	881.0	899.2
	V'	$3d^9\ 4f^1\ (5d\ 6s)^0$	885.8	904.1
	S	$3d^9\ 4f^1\ (5d\ 6s)^1$	895.7	914.0
Ce^{4+}	V_1	$3d^9\ 4f^1\ 5d^0\ 6s^0$	882.8	901.5
	V''	$3d^9\ 4f^0\ (5d\ 6s)^1$	889.0	907.4
	V'''	$3d^9\ 4f^0\ 5d^0\ 6s^0$	898.5	917.2

electrons in each J_z state. Herein, because the OQC-R structure and Ce–Ti–O-(3 × 3) superstructure are ultrathin films, we performed a determination by changing the angle (90° and 15°) between the incident X-ray and the surface normal to the specimen. The normalized XAS spectra of the Ce–Ti–O-(3 × 3) superstructure are shown in Fig. 4(c). Compared with the calculation results of previous studies,[20] we found that the wavefunction of the Ce 4f electrons is nearly in the $J_z = \pm 3/2$ state from the vertical axis rotation of the Ce–Ti–O-(3 × 3) superstructure. Moreover, the spatial distribution of the 4f electrons in the $J_z = \pm 3/2$ state shows that the Ce 4f electrons are polarized perpendicular to the Pt(111) substrate. Due to the 4f electrons, there will be interest in magnetism on the OQC-R structure and OQC structure in the future.

The surface phase diagram of the Ce–Ti–O ultrathin films on Pt(111) is shown in Fig. 5. It shows an overview of the surface phase structure covered with Ce and Ti, after post-annealing under UHV. Triangles, rounds, squares, and trapezoids mark the results based on the quantities we prepared in the experiments. However, these structures shown in Fig. 5 are summarized using the LEED pattern, so we could not confirm whether there are 3D islands on the surface. In addition to the OQC-R structure and Ce–Ti–O-(3 × 3) superstructure introduced above, three other LEED patterns were observed, as shown in Fig. 6. As shown in Fig. 6(a), when the initial Ti deposition is >2 ML, the w-TiO_x (w = wagon-wheel-like) structure is observed, owing to post-annealing under UHV.[21] With repeated annealing under UHV at 1000 °C, Ti gradually decreases, thus slowly transitioning to the Ce–Ti–O-(3 × 3) superstructure, then to the OQC-R structure. In between the transition, coexisting OQC-R and Ce–Ti–O-(1 × 1) spots can also be observed in the LEED pattern, as shown in Fig. 6(b). The 12 equidistant spots around the substrate lattice spots marked in yellow correspond to the OQC-R structure, while the spots marked in blue correspond to Ce–Ti–O-(1 × 1). Finally, the mixture would gradually change to the Pt(111)-($\sqrt{7} \times \sqrt{7}$)$R19°$ superstructure marked in white, while the Pt(111)-(1.4 × 1.4) structure corresponding to CeO_x marked in purple is also observed.[22] Notably, Ce and Ti atoms will gradually form the Ce–O or Ce–Ti–O 3D islands with annealing, which is irreversible. These 3D islands will not transform into a wetting layer like the Ba–Ti–O ultrathin films with annealing.

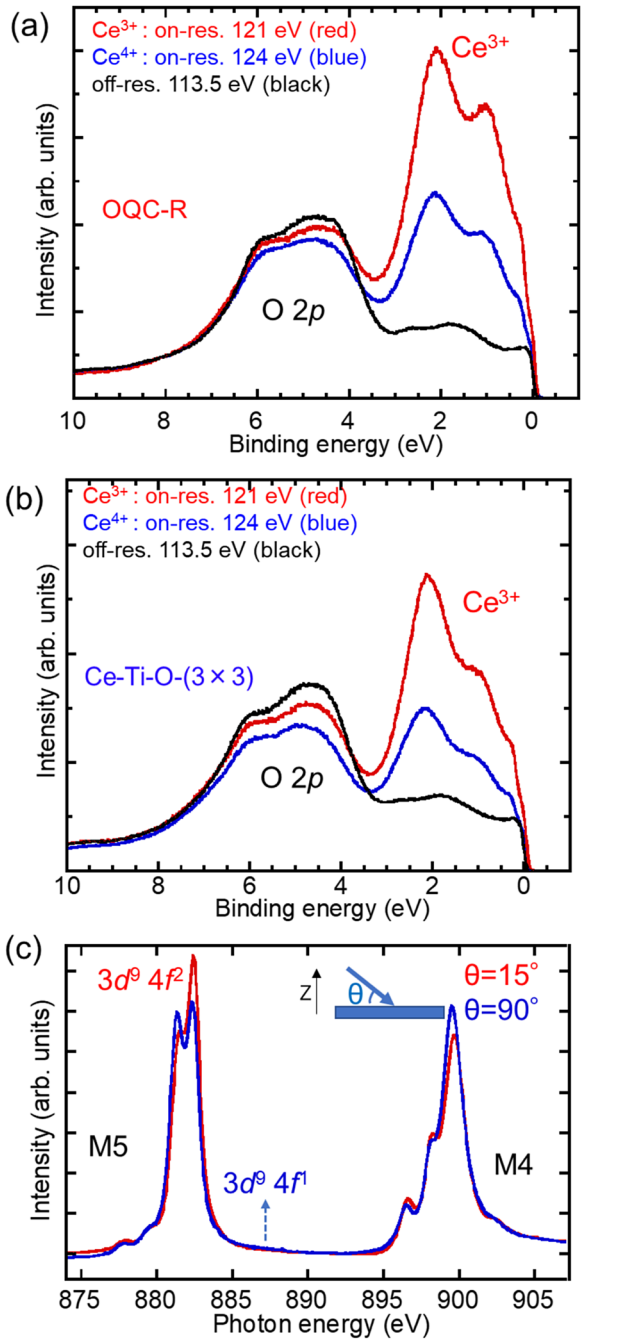

Fig. 4 The valence-band Ce 4d–4f resonant-PES spectra of the (a) OQC-R structure and (b) Ce–Ti–O-(3 × 3) superstructure. The resonant-PES spectra were measured with an excitation energy of 121 eV with resonant on (red), 124 eV with resonant on (blue), and 113.5 eV with resonant off (black), respectively. (c) The Ce 3d–4f (M-edge) XAS spectra of the Ce–Ti–O-(3 × 3) superstructure. The XAS spectra were measured with an angle of 15° (red) and 90° (blue) between the incident X-ray and the sample, as shown in the upper right.

IV Discussion

The structural models of the Ce–Ti–O-(3 × 3) superstructure and OQC-R structure are proposed, as shown in Fig. 7. A comparison of the structural parameters of the ultrathin Ce–Ti–O and Ba–Ti–O films on Pt(111) substrates is shown in Table 2. According to our previously proposed structural models for the OQC and OCA ultrathin Ba–Ti–O films,[8] the protrusions observed in the STM image are determined to be Ba atoms. Herein, the density

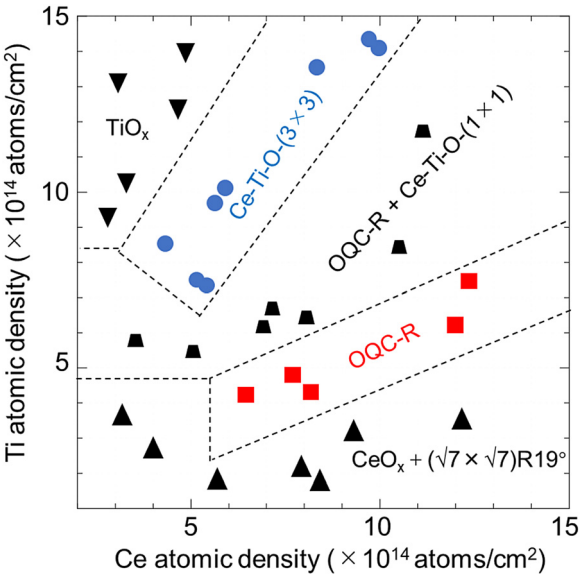

Fig. 5 Surface phase diagram of Ce–Ti–O thin films on Pt(111), as a function of Ce and Ti atomic density.

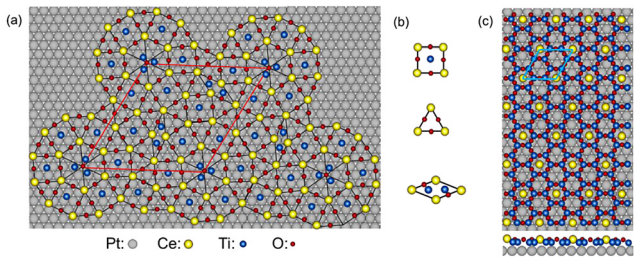

Fig. 7 The proposed structural models of the ultrathin Ce–Ti–O films. (a) The OQC-R structure. (b) The decoration of the square, triangle, and rhombus tiles in the OQC-R structure. (c) The Ce–Ti–O-(3 × 3) superstructure. Circles marked in gray, yellow, blue, and red indicate Pt, Ce, Ti, and O atoms, respectively. The unit cells of the OQC-R structure and Ce–Ti–O-(3 × 3) superstructure are marked in red and blue rhombus, respectively.

of protrusions in the OQC-R structure (1.8×10^{14} cm^{-2}) is higher than that in the Ce–Ti–O-(3 × 3) superstructure (0.7×10^{14} cm^{-2}) in the STM images. Compared with XPS and AES spectra, the OQC-R structure contains more Ce and less Ti than the Ce–Ti–O-(3 × 3) superstructure. Therefore, the protrusions observed in the STM image are mainly considered to be Ce atoms in both the OQC-R structure and Ce–Ti–O-(3 × 3) superstructure, and the reason for the reduced protrusions in the Ce–Ti–O-(3 × 3) superstructure is that Ce gathers to form the 3D island.

While the distorted Sigma phase is observed in Fig. 1(c), referring to Niizeki-Gähler tiling and Stampfli-Gähler tiling,[23–25] an idealized cluster without distortion is prepared in the structural model, as shown in Fig. 7(a). The decoration scheme for the three basic tiles in the OQC-R structure is shown in Fig. 7(b), where the gray, yellow, blue, and red spheres represent the Pt, Ce, Ti, and O atoms, respectively. Table 2 shows that the atomic density of Ce and Ti observed in the STM images of the OQC ultrathin Ba–Ti–O film is similar to that in the OQC-R ultrathin Ce–Ti–O film. Therefore, just like the Ba–Ti–O OQC structural model proposed before,[8] one Ti atom is located in the square and two Ti atoms are located in the rhombus, based on the symmetry of the structure and the composition ratios and atomic density calculated using the AES and XPS spectra. The triangles in the center of the dodecagon have different side lengths compared to the cluster, and they rotate in the opposite direction. Herein, they are not considered Ce atoms but are made of three Ti atoms, because these small triangles are not considered into the ideal tiling of the OQC-R structure. The O atoms are located between Ce atoms and among the three Ti atoms in the center of the dodecagon to balance its valence state. The stoichiometry of this structural model was $Ce_{18}Ti_{14}O_{41}$ per unit cell, which is also consistent with the valence state, while Ce and Ti correspond to Ce^{3+} and Ti^{2+} states, respectively. The elemental atomic densities for Ce, Ti, and O atoms are determined to be 1.5×10^{14}, 1.2×10^{14}, and 3.4×10^{14} atoms per cm^2, respectively. Although the OQC structure from the ultra-thin Ce–Ti–O film has not been observed yet, the ideal tiling of the OQC-R structure could provide the possibilities of discovering new oxide quasicrystals with rare earth elements.

The model of a simple Ce–Ti–O-(3 × 3) honeycomb superstructure is proposed, as shown in Fig. 7(c). This structural model is also consistent with the valence state of each element observed in the XPS spectra, where Ce corresponds to the Ce^{3+}

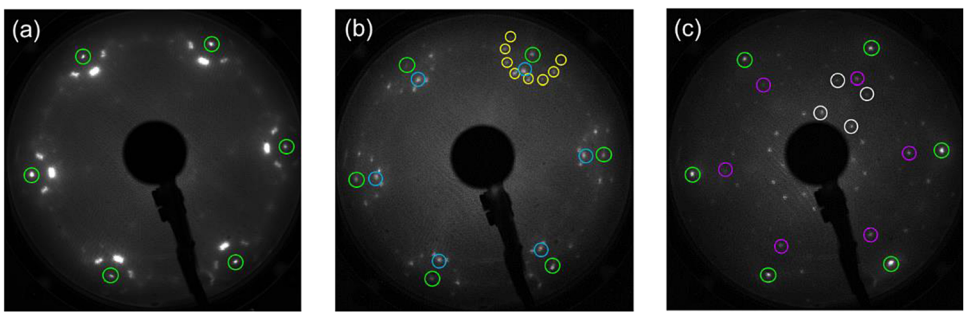

Fig. 6 LEED patterns (66 eV) of ultrathin Ce–Ti–O films on Pt(111) in the surface phase diagram (a) w-TiO_x, (b) OQC-R + Ce–Ti–O-(1 × 1), and (c) Pt(111)-(1.4 × 1.4) + Pt(111)-($\sqrt{7} \times \sqrt{7}$)$R19°$. The OQC-R spots are marked with yellow circles, the Ce–Ti–O-(1 × 1) spots are marked with blue circles, the Pt(111)-(1.4 × 1.4) spots are marked with purple circles, and the Pt(111)-($\sqrt{7} \times \sqrt{7}$)$R19°$ spots are marked with white circles.

Table 2 Structural parameters of OQC-R and Ce–Ti–O-(3 × 3) ultrathin films obtained for Ce–Ti–O/Pt(111), and σ-phase OCA and OQC ultrathin films obtained for Ba–Ti–O/Pt(111): the composition ratios, the average distance of protrusions, the density of protrusions, and atomic density in the experiment, as well as the stoichiometry and atomic density in the proposed structural models

		Ce–Ti–O ultrathin films		Ba–Ti–O ultrathin films[7,8]	
		OQC-R	Ce–Ti–O-(3 × 3)	OQC	σ-phase OCA
Composition ratios from AES		(Ce : Ti : O) 1.0 : 0.3 : 0.8	(Ce : Ti : O) 1.0 : 0.8 : 1.6	(Ba : Ti : O) 1.0 : 0.3 : 0.8	(Ba : Ti : O) 1.0 : 0.6 : 1.2
Average distance of protrusions in the STM (nm)		0.64	0.99	0.69	0.67
Rotation of unit cell with Pt(111)		2°	0°	—	8°
Number density of protrusions in STM ($\times 10^{14}$ cm^{-2})		1.8	0.7	2.8	2.4
Atomic density from XPS and RBS ($\times 10^{14}$ atoms per cm^2)	Ce/Ba	8 ± 3	5 ± 3	7 ± 3	8 ± 3
	Ti	4 ± 2	7 ± 2	4 ± 2	6 ± 2
	O	5 ± 1	8 ± 1	3 ± 1	4 ± 1
Stoichiometry in structural models		$Ce_{18}Ti_{14}O_{41}$	$CeTi_6O_9$	$Ba_{12}Ti_5O_{12}$	$Ba_4Ti_4O_{10}$
Atomic density in structural models ($\times 10^{14}$ atoms per cm^2)	Ce/Ba	1.5	0.7	2.8	2.4
	Ti	1.2	4.2	1.2	2.4
	O	3.4	6.3	2.8	5.9

state, and Ti corresponds to the Ti^{3+} and Ti^{2+} states. The stoichiometry of this honeycomb structural model was $CeTi_6O_9$ per unit cell. The model determines the elemental atomic densities for Ce, Ti, and O atoms to be 0.7 × 10^{14}, 4.2 × 10^{14}, and 6.3 × 10^{14} atoms per cm^2, respectively. The atomic density in the Ce–Ti–O-(3 × 3) structural model differs from the experimental atomic density estimated from the XPS spectra because of 3D islands, as observed in the STM image. A report by Schenk *et al.*[26] proposed a 2/3 Ba-decorated Ti_2O_3 honeycomb structural model and all Ba decorated Ti_2O_3 σ-phase structural models. Stone–Wales transformation converts the honeycomb structure into square-triangle tiling and rhombus formation using the adjoining O. Therefore, the honeycomb structure could be somehow related to the OQC structure. It could be known from experiments that after Ti deposition on the OQC-R structure, with oxidation, the Ce–Ti–O-(3 × 3) honeycomb superstructure is prepared. This is also reflected in the structural models. For the OQC-R structure with less O and Ti, each Ce atom was surrounded by 2–3 Ti atoms and 3–5 O atoms, while there were six O atoms and six Ti atoms around cerium in the Ce–Ti–O-(3 × 3) honeycomb superstructure.

Perovskites are known for their extraordinary diversity of magnetism. According to a study based on density functional theory by Dorini *et al.*,[27] the magnetism remains even in single atomic layers. Although the Ba–Ti–O and Sr–Ti–O structures have no magnetic properties, the Ce–Ti–O structure was reported by Li *et al.*[28] to show magnetism up to 400 K. Also, it is important to note that superconductivity in the Ti–O structures is reported to be present in a Ti^{2+} system,[29] Ti^{3+} system,[30] and mixed Ti^{3+}/Ti^{4+} system.[31] Also, as we know, the famous Mermin–Wagner theorem states that continuous symmetries cannot be broken spontaneously in 2D (or 1D) systems.[32] However, there are also some works in quasicrystals that seem to contradict the Mermin–Wagner theorem.[33,34] We have not yet analysed the magnetic properties of Ce–Ti–O ultrathin films in experiment. However, we think that the discovery of the OQC-R structure of the Ce–Ti–O ultra-thin film provides the possibility of discovering new OQCs with rare earth metals, and their novel magnetism or superconductivity may be found.

V Conclusions

A OQC-R structure and a Ce–Ti–O-(3 × 3) honeycomb superstructure on the Pt(111) substrate were successfully prepared using Ce and Ti depositions, followed by annealing in an O_2 atmosphere and UHV. The OQC-R structure with a dodecagonal cluster is observed in the STM image. For the OQC-R structure, Ce and Ti correspond to the Ce^{3+} and Ti^{2+} states, respectively. In addition, Ce corresponds to the Ce^{3+} state, and Ti corresponds to Ti^{3+} and Ti^{2+} states for the Ce–Ti–O-(3 × 3) honeycomb superstructure. These two structures are quantitatively analyzed using LEED, STM, AES, XPS, and RBS. The results show that the OQC-R structure can be converted into a honeycomb (3 × 3) structure by increasing the Ti and O content. The valence states and atomic density have proposed relevant ideal possible schematic structural models of the two structures, where the Ce atoms occupy the tiling corners. The discovery of the OQC-R structure with a magnetic rare earth metal also provides the possibilities of the discovery of new oxide quasicrystals with novel magnetism or superconductivity.

Conflicts of interest

There are no conflicts to declare.

Acknowledgements

The authors thank Wolf Widdra for his enthusiasm and advice on the structural models. This work was partially supported by a Grant-in-Aid for Scientific Research on Innovative Areas ''Hypermaterials: Innovation of materials science in hyperspace'' (Grant No. 20H05267 and 22H04588) from the Ministry of Education, Culture, Sports, Science, and Technology (MEXT). This work was financially supported by JST SPRING, grant number JPMJSP2125. XL would like to take this opportunity to thank the ''Interdisciplinary Frontier Next-Generation Researcher Program of Tokai Higher Education and Research System.'' XL acknowledges financial support from the Sasakawa Scientific Research Grant from The Japan Science Society in

2022. JY acknowledges financial support from the Suzuki Foundation in 2023.

References

1 D. Shechtman, I. Blech, D. Gratias and J. W. Cahn, *Phys. Rev. Lett.*, 1984, **53**, 1951–1953.
2 S. Förster, K. Meinel, R. Hammer, M. Trautmann and W. Widdra, *Nature*, 2013, **502**, 215–218.
3 S. Schenk, S. Förster, K. Meinel, R. Hammer, B. Leibundgut, M. Paleschke, J. Pantzer, C. Dresler, F. O. Schumann and W. Widdra, *J. Phys.: Condens. Matter*, 2017, **29**, 134002.
4 S. Förster, M. Trautmann, S. Roy, W. A. Adeagbo, E. M. Zollner, R. Hammer, F. O. Schumann, K. Meinel, S. K. Nayak, K. Mohseni, W. Hergert, H. L. Meyerheim and W. Widdra, *Phys. Rev. Lett.*, 2016, **117**, 095501.
5 E. Maria Zollner, F. Schuster, K. Meinel, P. Stötzner, S. Schenk, B. Allner, S. Förster and W. Widdra, *Phys. Status Solidi B*, 2020, **257**, 1900655.
6 F. E. Wührl, O. Krahn, S. Schenk, S. Förster and W. Widdra, *Phys. Status Solidi B*, 2022, **259**, 2100389.
7 J. Yuhara, K. Horiba, R. Sugiura, X. Li and T. Yamada, *Phys. Rev. Mater.*, 2020, **4**, 103402.
8 X. Li, K. Horiba, R. Sugiura, T. Yamada and J. Yuhara, *Appl. Surf. Sci.*, 2021, **561**, 150099.
9 C. R. Merchan, T. T. Dorini, F. Brix, L. Pasquier, M. Jullien, D. Pierre, S. Andrieu, K. Dumesnil, S. S. Parapari, S. Šturm, J. Ledieu, M. Sicot, O. Copie, E. Gaudry and V. Fournée, *Phys. Chem. Chem. Phys.*, 2022, **24**, 7253–7263.
10 M. Maniraj, L. V. Tran, O. Krahn, S. Schenk, W. Widdra and S. Förster, *Phys. Rev. Mater.*, 2021, **5**, 084006.
11 P. Ghising, D. Das, S. Das and Z. Hossain, *J. Phys.: Condens. Matter*, 2018, **30**, 285002.
12 T. Ueda, H. Shishido, S. Hashimoto, T. Okubo, M. Yamada, Y. Inada, R. Settai, H. Harima, A. Galatanu, E. Yamamoto, N. Nakamura, K. Sugiyama, T. Takeuchi, K. Kindo, T. Namiki, Y. Aoki, H. Sato and Y. Onuki, *J. Phys. Soc. Jpn.*, 2004, **73**, 649–655.
13 N. Takeda and M. Ishikawa, *J. Phys. Soc. Jpn.*, 2000, **69**, 868–873.
14 L. H. Chan and J. Yuhara, *J. Chem. Phys.*, 2015, **143**, 074708.
15 T.-M. Pan, T.-Y. Wu, C.-L. Chan and S.-T. Pang, *Ceramics Int.*, 2018, **44**, 12528–12534.
16 K.-D. Schierbaum, *Surf. Sci.*, 1998, **399**, 29–38.
17 K. S. Sim, L. Hilaire, F. L. Normand, R. Touroude, V. Paul-Boncour and A. Percheron-Guegan, *J. Chem. Soc., Faraday Trans.*, 1991, **87**, 1453–1460.
18 V. V. Atuchin, V. G. Kesler, N. V. Pervukhina and Z. Zhang, *J. Electron Spectrosc. Relat. Phenom.*, 2006, **152**, 18–24.
19 S. Imada, A. Sekiyama and S. Suga, *Jpn. Soc. Appl. Phys. Int.*, 1998, **11**, 212–214.
20 P. Hansmann, A. Severing, Z. Hu, M. W. Haverkort, C. F. Chang, S. Klein, A. Tanaka, H. H. Hsieh, H.-J. Lin, C. T. Chen, B. Fåk, P. Lejay and L. H. Tjeng, *Phys. Rev. Lett.*, 2008, **100**, 066405.
21 F. Sedona, G. A. Rizzi, S. Agnoli, F. X. Llabrés, I. Xamena, A. Papageorgiou, D. Ostermann, M. Sambi, P. Finetti, K. Schierbaum and G. Granozzi, *J. Phys. Chem. B*, 2005, **109**, 24411–24426.
22 C. Hardacre, G. M. Roe and R. M. Lambert, *Surf. Sci.*, 1995, **326**, 1–10.
23 F. Gähler, *Quasicrystals*, ed C. Janot and R. Mosseri, World Scientific, Singapore, 1995.
24 J. Hermisson, C. Richard and M. Baake, *J. Phys. I*, 1997, **7**, 1003–1018.
25 K. Niizeki, *J. Phys. A: Math. Gen.*, 1988, **21**, 2167.
26 S. Schenk, O. Krahn, E. Cockayne, H. L. Meyerheim, M. de Boissieu, S. Förster and W. Widdra, *Nat. Commun.*, 2022, **13**, 7542.
27 T. T. Dorini, F. Brix, C. Chatelier, A. Kokalj and É. Gaudry, *Nanoscale*, 2021, **13**, 10771–10779.
28 J. Li, A. Gong, X. Li, Y. He, J. Li, Y. Bai and R. Fan, *RSC Adv.*, 2022, **12**, 15348–15353.
29 C. Zhang, F. Hao, G. Gao, X. Liu, C. Ma, Y. Lin, Y. Yin and X. Li, *npj Quant. Mater.*, 2017, **2**, 2.
30 Y. Li, Y. Weng, J. Zhang, J. Ding, Y. Zhu, Q. Wang, Y. Yang, Y. Cheng, Q. Zhang, P. Li, J. Lin, W. Chen, Y. Han, X. Zhang, L. Chen, X. Chen, J. Chen, S. Dong, X. Chen and T. Wu, *NPG Asia Mater.*, 2018, **10**, 522–532.
31 K. Yoshimatsu, O. Sakata and A. Ohtomo, *Sci. Rep.*, 2017, **7**, 12544.
32 N. D. Mermin and H. Wagner, *Phys. Rev. Lett.*, 1966, **17**, 1133–1136.
33 L. Leuzzi and G. Parisi, *J. Phys. A: Math. Gen.*, 2000, **33**, 4215.
34 Z. Rotman and E. Eisenberg, *Phys. Rev. E: Stat., Nonlinear, Soft Matter Phys.*, 2011, **83**, 011123.

